



Ultrathin manganese oxides enhance the electrocatalytic properties of 3D printed carbon catalysts for electrochemical nitrate reduction to ammonia

Wanli Gao^a, Juan V. Perales-Rondon^a, Jan Michalička^a, Martin Pumera^{a,b,c,d,*}

^a Future Energy and Innovation Laboratory, Central European Institute of Technology, Brno University of Technology (CEITEC-BUT), Purkyňova 123, 61200 Brno, Czech Republic

^b Department of Chemical and Biomolecular Engineering, Yonsei University, 50 Yonsei-ro, Seodaemun-gu, Seoul 03722, South Korea

^c Faculty of Electrical Engineering and Computer Science, VSB - Technical University of Ostrava, 17. listopadu 2172/15, 70800 Ostrava, Czech Republic

^d Department of Medical Research, China Medical University Hospital, China Medical University, No. 91 Hsueh-Shih Road, Taichung 40402, Taiwan

ARTICLE INFO

Keywords:

3D printing
Atomic layer deposition
Carbon materials
Manganese oxides
Ammonia
Electrocatalysts

ABSTRACT

Electrochemical nitrate reduction reaction (NO₃RR) is a promising approach to remedying the environmental pollution from nitrate, and simultaneously a sustainable alternative to traditional Haber-Bosch process especially for decentralized ammonia production. Here, we firstly explore the electrocatalytic activity of two 3D printed carbon frameworks consisting of 0-dimensional (0D) carbon black and 1-dimensional (1D) carbon nanotubes towards cost-efficient electrocatalysts for NO₃RR. Different from the electrocatalytic inert properties of 0D carbon framework, 1D carbon framework exhibits the electrocatalytic activity for NO₃RR with a Faradaic efficiency of more than 50% at −1.21 V vs. RHE. Control experiments suggest that such activity originates from the synergistic electrocatalytic contributions between intrinsic surface features of carbon nanotubes and metallic impurities. Since the content and distribution of these metallic impurities are unpredictable, an ultrathin deposit of electrocatalytic manganese oxides is further deposited by atomic layer deposition on 1D carbon framework to ensure well defined surfaces for effective NO₃RR. The proposed strategy by integrating 3D printing of conductive carbon framework with atomic layer deposition of an electrocatalytic layer provides a feasible electrode fabrication for electrochemical NO₃RR and shows a promising prospect in the electrocatalytic field.

1. Introduction

Ammonia (NH₃) is one of the most essential chemicals for the global agriculture and industry, and is also regarded as an important energy storage medium and green energy carrier due to its high hydrogen storage capacity [1–4]. Ammonia has traditionally been produced by the well-known Haber-Bosch (HB) process ($N_2 + 3 H_2 \rightarrow 2NH_3$), in which high temperatures and pressures are rigorously required [5]. Such reaction process demands a high consumption of global energy supply from fossil fuels, and consequently contributes to a significant generation of carbon dioxide (CO₂), which is a handicap for its future applications in terms of cost efficiency and environmental sustainability. Therefore, research efforts have been devoted to searching for sustainable alternatives to HB process.

Owing to the use of electricity from renewable sources such as solar and wind energy, electrochemical NO₃RR under mild conditions has

boosted growing scientific efforts for decentralized NH₃ production with potential of simultaneously remedying the nitrate pollution [6–14]. Implementation of electrochemical NO₃RR for NH₃ production requires the development of effective and cost-efficient electrocatalysts for this eight-electron reaction [15,16]. To date, significant attention has been focused on metal-based catalysts for electrochemical NO₃RR, incorporating monometallic materials [17–24], metal oxides [25–30], and bimetallic materials [31–34]. In a sharp contrast, although carbon materials have demonstrated their effectiveness as low-cost electrocatalysts for other electrochemical reactions, such as hydrogen evolution reaction (HER), oxygen evolution reaction (OER), and oxygen reduction reaction (ORR) [35], and have been commonly served as the conductive substrate to support NO₃RR catalysts [32,36], yet they remain less explored towards electrochemical NO₃RR [37–40]. The use of carbon materials for conductive substrate was exemplified by loading graphite paper with CoO nanoparticle decorated N-doped carbon nanotubes, which enables

* Corresponding author at: Future Energy and Innovation Laboratory, Central European Institute of Technology, Brno University of Technology (CEITEC-BUT), Purkyňova 123, 61200 Brno, Czech Republic.

E-mail address: martin.pumera@ceitec.vutbr.cz (M. Pumera).

<https://doi.org/10.1016/j.apcatb.2023.122632>

Received 9 October 2022; Received in revised form 23 February 2023; Accepted 12 March 2023

Available online 14 March 2023

0926-3373/© 2023 Elsevier B.V. All rights reserved.

a good dispersion of CoO and simultaneously provides effective conductive pathways for effective NO₃RR [41]. Another example was presented by encapsulating Fe₃C nanoparticles into N-doped carbon nanotubes as a bifunctional catalyst with core-shell structure for NO₃RR and electrocatalytic oxidation of H₂S to S [42]. The few direct studies on carbon materials for NO₃RR have indicated that the surface of pristine carbon nanotubes and graphene is electrocatalytically active [38,43], showing their potential as solely used electrocatalyst for NO₃RR. Therefore, there is a compelling need to further investigate the activity of cost-efficient carbon materials and understand their active sites for NO₃RR.

Apart from the intrinsic activity of electrocatalysts, a rational design of electrode structures with high specific surface area to favorably expose the catalytic active sites is another key aspect to obtain the optimum electrocatalytic performance. Such electrode design can be readily realized by 3-dimensional (3D) printing, which enables an on-demand electrode fabrication with accurately controlled geometry and structure [44–46]. Among various 3D printing processes, fused deposition modelling (FDM) 3D printing has attracted increasing scientific and industrial attention due to its high manufacturing efficiency, low cost, simplicity, and easily accessible large size capability. By using the industrially available carbon filaments, FDM 3D printed carbon frameworks have sparked a growing interest in the fabrication of electrodes for electrocatalysis, as exemplified by 1D carbon nanotubes containing metallic impurities [47,48]. These 1D carbon frameworks are analogue to metallic impurities coupled carbon substrates, and electrocatalytic activities are commonly ascribed to the metallic impurities [47–50], which are primarily from the metal catalyst nanoparticles used in the production of carbon nanotubes [51,52]. However, such electrocatalytic activity originated from impurities of 3D printed carbon frameworks cannot be well controlled, varying from different industrial fabrication processes. In light of this, a complementary surface engineering technique for the fine-tuning of the surface chemistry of 3D printed carbon frameworks is highly desired. To this end, atomic layer deposition (ALD) stands out as a compatible coating technique to functionalize 3D printed carbon frameworks with the atomic-precision active layers by sequential, self-limiting surface reactions [53–55], which ensures the electrocatalytic reproducibility of the 3D printed carbon frameworks without compromise of their initial porosity. Therefore, a well-defined structure consisting of conductive core and ultrathin shell can be obtained by integrating ALD of active materials with 3D printing of conductive carbon substrates. Such core-shell structure is of particular interest for electrocatalytic applications since it can provide (i) the sufficient exposure of active materials to the electrolyte, as well as (ii) the effective electron transfer from conductive carbon substrate to ultrathin active materials. Mn-incorporated catalysts have shown their electrocatalytic activity in many electrochemical reactions, yet their application to NO₃RR has been less reported [30,56]. Besides, the ALD of manganese oxides (MnO_x) can be realized at a relatively low temperature [53]. This makes it possible for ALD of MnO_x for NO₃RR on 3D printed carbon framework, since high temperature should be avoided during ALD process to suppress the pyrolysis of polylactic acid (PLA) in 3D printed carbon framework, which plays an essential role in keeping the mechanical integrity of 3D printed structures.

Inspired by the recent advances in 3D printed carbon electrocatalysts [48], in this work, we firstly explore the electrochemical NO₃RR activity of 3D printed carbon frameworks using two commercial carbon materials, represented by 0D carbon black [57], and 1D carbon nanotubes [58]. Unlike the inert catalytic behavior of 0D counterpart, 1D carbon framework demonstrates the electrocatalytic activity towards electrochemical NO₃RR, which is ascribed to the synergistic electrocatalytic contributions between intrinsic surface features of carbon nanotubes and metallic impurities. Furthermore, ALD is introduced as a compatible technique with 3D printing for the fabrication of electrocatalytic active manganese oxides (MnO_x) functionalized carbon frameworks. Importantly, since the ALD-coated layer can effectively modify the surface

chemistry of 3D printed carbon frameworks, this combined technique provides a promising fabrication strategy for electrocatalytic carbon frameworks with on-demand architectures.

2. Experimental section

2.1. 3D-printing of carbon frameworks and post-printing activation

Autodesk fusion 360 software was used to create a circular disc with a diameter and a thickness of 9 mm and 0.45 mm, respectively. A connecting strip was designed with each disc for a connection to the working electrode by crocodile clip. The designed file was then sliced and exported as G-code file via Prusa-Slicer software. Based on the G-code file, 3D printing was performed on Prusa i3 MK3 printer (Prusa Research, Czech Republic) with two commercially available conductive carbon filaments, in which 0D carbon black (ProtoPasta, ProtoPlant, Inc., USA) and 1D carbon nanotubes (BlackMagic, Graphene Supermarket, USA) are used as conductive fillers. The nozzle temperature was respectively set to 215 °C and 230 °C for 0D and 1D carbon framework printing, and the bed temperature was kept constant at 60 °C. The as-printed carbon frameworks were immersed into 1 M NaOH for 3 h to partially remove the surficial PLA through chemical saponification reaction, then rinsed with deionized water and dried in the air.

2.2. Atomic layer deposition of MnO_x

The MnO_x was grown in an oxygen plasma atomic layer deposition system (ALD, Ultratech/CambridgeNanoTech Fiji 200), in which Tris (2,2,6,6-tetramethyl-3,5-heptanedionato)manganese(III) (Mn(TMHD)₃, 99%, Strem Chemicals) was used as Mn precursor. The stainless steel cylinder for Mn precursor was kept at 135 °C for vapor pressure without decomposition. The argon carrier boost gas was pulsed through the Mn precursor cylinder to introduce sufficient Mn precursor to the ALD chamber. Oxygen under the plasma power of 300 W was used as the reactant gas. Argon was used as the carrier gas at the rate of 50 sccm for Mn precursor and 55 sccm for O₂ plasma throughout the deposition. The ALD chamber was heated to 150 °C and stabilized for 30 min before deposition. To obtain the MnO_x deposit with different thickness on 1D carbon framework, the deposition was performed for 100, 300, and 500 cycles. The corresponding samples were designated as 1D@ 100-, 1D@ 300-, and 1D@ 500-MnO_x, respectively. Each ALD cycle consists of 0.5 s precursor pulse, 0.5 s argon boost pulse, 5 s purging, 20 s oxygen plasma exposure, and another 5 s purging.

2.3. Preparation of TiO₂ and Fe₃O₄ electrodes

2 mg of TiO₂ (Sigma Aldrich) or Fe₃O₄ (Sigma Aldrich) powder, 0.5 mL H₂O, 0.5 mL ethanol (96%), and 10 μL Nafion (Sigma Aldrich, 5 wt %) were mixed in a plastic vial and sonicated for 3 h to get a quasi-homogeneous suspension. Then a total volume of 6 μL suspension was drop-coated on the glassy carbon electrode (0.071 cm²), and dried in the air. The pyrolytic graphite electrode (0.071 cm²) with basal (PGEb) and edge orientation (PGEe) were purchased from BAS, Inc. (Japan) and used as received for electrocatalytic measurements to study the effect of carbon defects on the electrochemical NO₃RR of carbon nanotubes.

2.4. Characterizations

Scanning electron microscopy (SEM) was performed by SEM Verios 460 L (Thermo Fisher Scientific (TFS), USA) with an electron beam accelerating voltage of 5 kV. Elemental mapping was obtained by energy-dispersive X-ray (EDX) spectroscopy integrated in the SEM (Lyra) with accelerating voltage of 20 kV. Nano-characterization was carried out on an image-corrected and monochromated TEM Thermo-fisher Scientific TITAN Themis 60–300 equipped with HAADF STEM imaging detector, Super-X EDX spectrometer, and Gatan GIF Quantum

ERS EELS spectrometer. The microscope was operated at accelerating voltage of 300 kV for STEM-HAADF high resolution imaging and for STEM-EDX mapping, and 60 kV for STEM-EELS analysis to mitigate the beam damage to the nanoclusters' structure and chemistry. Velox software version 2.12 was used to acquire and process the STEM-EDX data and DigitalMicrograph software version 3.2 was used to acquire and process EELS data. STEM-EDX elemental mapping was performed in net intensities with the use of maximum likelihood fit method for the deconvolution of overlapping peaks and empirical model for spectrum background subtraction. X-ray photoelectron spectroscopy (XPS) was carried out on an AXIS Supra instrument (Kratos Analytical, UK) using monochromatized Al K α excitation source (1486.7 eV). The manganese (Mn) content was evaluated by inductively coupled plasma optical emission spectrometry (IPC-OES, Arcos MV, SPECTRO Analytical Instruments, Kleve, Germany). A detailed procedure for IPC-OES measurements is described in the [Supporting Information](#).

2.5. Electrochemical measurements

The electrolysis was performed in an H-type glass cell separated by a frit in ambient environment. The electrochemical signal was recorded by an AutoLab workstation (PGSTAT204, Metrohm). A commercial Ag/AgCl (filled with KCl gel electrolyte) and platinum wire were used as reference and counter electrode, respectively. A solution of 0.1 M KNO₃/0.5 M Na₂SO₄ was used for electrocatalytic measurements, and was evenly distributed to the anodic and cathodic compartment (20 mL for each). The electrocatalytic measurements were carried out at selected potentials for 1 h at a magnetic stirring rate of 175 rpm to investigate the ammonia yield and Faraday efficiency (FE) of different catalysts. The linear sweep voltammetry (LSV) tests were performed at a scan rate of 5 mV s⁻¹ to preliminarily probe the NO₃RR performance of different electrodes. The electrochemically active surface area (ECSA) of PGEb and PGEe electrodes was calculated from the electrochemical double-layer capacitance (C_{DL}), which was obtained by recording the cyclic voltammetry responses in 0.5 M Na₂SO₄ at different scan rates within a non-Faradaic potential range. All applied potentials were converted to the reversible hydrogen electrode (RHE) scale based on the equation: E (vs. RHE) = E (vs. Ag/AgCl) + 0.059 V × pH + 0.199 V. All electrolysis tests were repeated three times to ensure reliability.

2.6. Determination of ammonia

The NH₃ concentration after each electrocatalytic test was detected by ultraviolet-visible (UV-vis) spectrophotometer (JASCO V-750). Specifically, a certain amount of solution was taken out from the electrolytic cell and diluted to an appropriate detection range up to 600 μ L. A solution consisting of 3 M NaOH, 10 wt% salicylic acid, and 10 wt% sodium citrate (600 μ L) was firstly added to the diluted solution, followed by the sequential addition of 0.20 M NaClO (300 μ L) and 2.0 wt% sodium nitroferricyanide (60 μ L). The mixed solution was placed for 2 h prior to UV-vis spectrophotometry measurements. The contents of formed indophenol blue product were calculated by the absorbance at a wavelength of 655 nm based on the calibration curve [22], which was obtained by measuring the absorbance of a series of standard NH₄Cl solutions with 0.5 M Na₂SO₄.

Calculation of the FE and NH₃ yield rate: The FE and NH₃ yield rate (r_{NH_3}) were calculated based on the following equations:

$$FE = (8F \times c_{\text{NH}_3} \times V) / Q \quad (1)$$

$$r_{\text{NH}_3} = (c_{\text{NH}_3} \times V) / (t \times S) \quad (2)$$

where F is the Faradaic constant (96485 C mol⁻¹), c_{NH_3} is the concentration of measured NH₃, V is the electrolyte volume of the cathodic compartment, Q is the total charge passing the electrode, t is the reaction time, and S is the geometric area of working electrode.

2.7. Determination of nitrite

The color reagent for NO₂⁻ detection was prepared by mixing N-(1-Naphthyl) ethylenediamine dihydrochloride (0.02 g), sulfanilamide (0.4 g), ultrapure water (5 mL), and phosphoric acid (1 mL, $\rho = 1.70$ g/mL). Specifically, a certain amount of solution was taken out from the electrolytic cell and diluted to an appropriate detection range up to 1.5 mL. Then, 50 μ L of color reagent was added into the aforementioned 1.5 mL solution. The mixed solution was rested for 20 min prior to UV-vis spectrophotometry measurements. The NO₂⁻ concentration was calculated by the absorbance at a wavelength of 540 nm based on the calibration curve, which was obtained by a series of standard NaNO₂ solutions with 0.5 M Na₂SO₄.

2.8. Determination of ammonia by ¹H NMR (isotopic labelling experiment)

For the isotopic labeling experiment, an electrolytic experiment was carried out with an initial concentration of K¹⁵NO₃ 0.1 M. After the electrolysis, the catholyte was taken out from the cell. 250 μ L of concentrated H₂SO₄ was added to 5 mL of catholyte to adjust the pH value to be acid for quantification by ¹H NMR (500 MHz). Additionally, 0.002 g of maleic acid was added as internal standard. After that, 500 μ L of this solution was placed in an NMR tube and 50 μ L deuterium oxide (D₂O) was added for the NMR detection.

3. Results and discussion

3.1. Characterization and electrochemical NO₃RR performance of 0D and 1D carbon framework

The 3D printed 0D and 1D carbon frameworks were activated by partially removing surficial insulating PLA to expose the carbon catalysts for electrochemical NO₃RR. SEM images of 0D (Fig. 1a and b) carbon framework display a macroporous structure consisting of carbon black particles with typical aggregates size less than 1 μ m. Similarly, 1D carbon framework shows a porosity formed by interconnected carbon nanotubes with diameter of tens to a few hundreds of nanometers (Fig. 1d and e). The bulk chemical compositions by EDX reveal the existence of metallic impurities (Ti, Fe) in 1D carbon framework apart from S (Fig. 1f) compared to its 0D counterpart (Fig. 1c). Furthermore, elemental mapping shows the roughly uniform distribution of these impurities in 1D carbon framework (Fig. 1g). Additionally, the content of impurities in carbon frameworks was quantitatively analysed by IPC-OES measurements. In line with the EDX results, no metallic impurities exist in 0D carbon framework, whereas a considerable amount of metallic impurities are detected in 1D carbon framework (Fig. 1h). For example, Ti accounts for a dominant amount of more than 1 wt%, followed by Fe, which have been demonstrated to originate from TiO₂ and Fe₃O₄, respectively [47,48]. More detailed analysis of scanning transmission electron microscopy with EDX (STEM-EDX) further reveals the presence of TiO₂ particle aggregates with lateral size of ~ 10 to ~ 20 nm on the surface of carbon nanotubes (Fig. S1). To verify the surficial chemical compositions of carbon frameworks, XPS was employed (Fig. 1i, j). 1D carbon framework clearly presents Ti impurities signal but no recognizable Fe signal is observed. This indicates that the trace Fe₃O₄ impurities are not sufficiently exposed on the surface of 1D carbon framework, which cannot be effectively identified by XPS due to their low content and detection limitations of XPS [59]. however, it is worth emphasizing that although Fe₃O₄ impurities are not detected by XPS, it is still possible to exert a considerable catalytic effect to 1D carbon framework. This is similar to single-atom catalysts, which can be clearly identified by bulk-related characterizations but hardly detected by surface-sensitive XPS [22,60]. Therefore, the catalytic influence from Fe₃O₄ on 1D carbon framework should not be neglected and the electrochemical NO₃RR properties of both TiO₂ and Fe₃O₄ impurities were

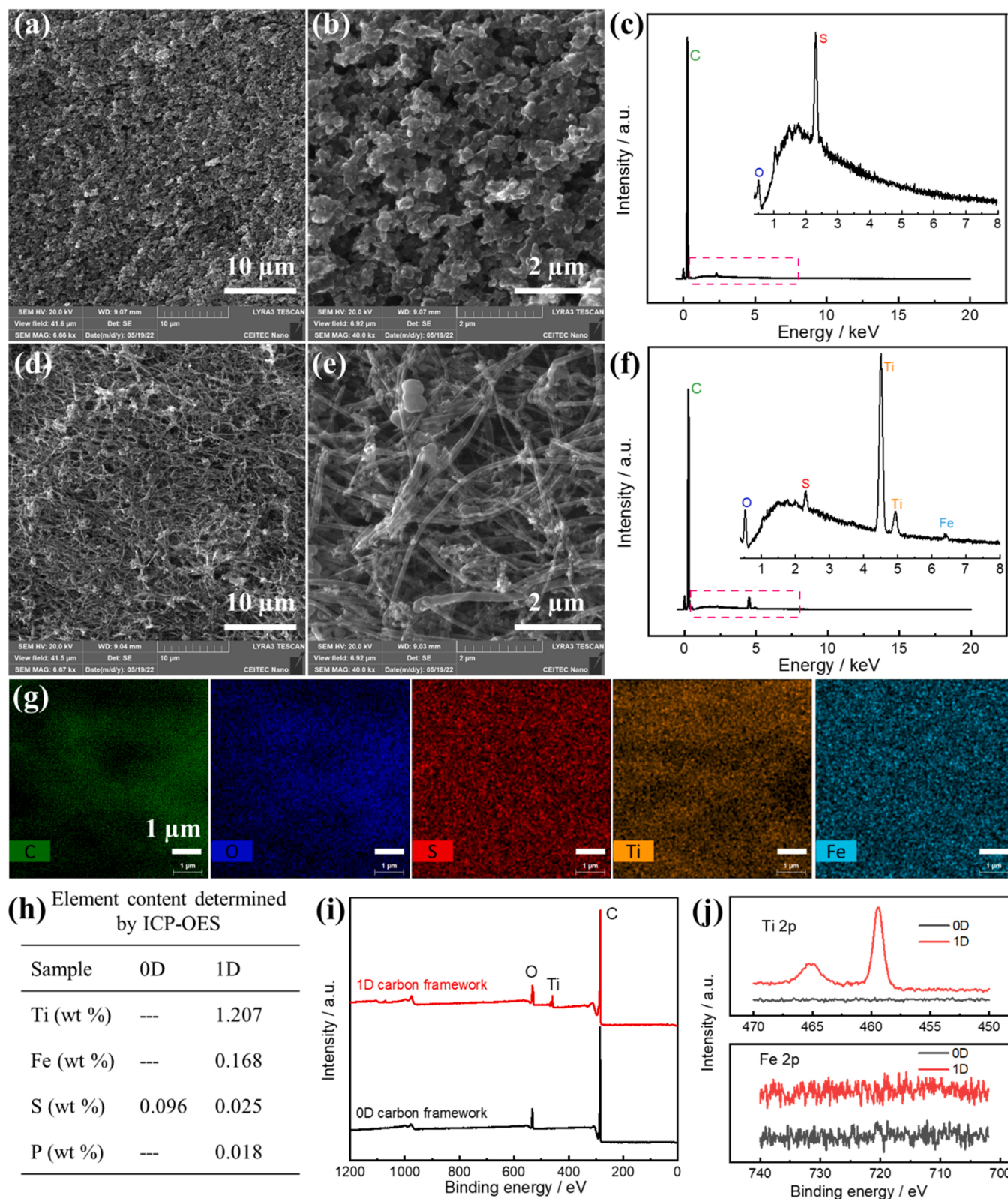


Fig. 1. (a, b) SEM images of 0D carbon framework. (c) EDX spectrum of 0D carbon framework performed on the area of (b). (d, e) SEM images of 1D carbon framework. (f) EDX spectrum of 1D carbon framework performed on the area of (e), together with its elemental mapping (g). (h) The element content analysis by ICP-OES, in which the elements with weight content lower than 0.01 wt% are not considered. (i) XPS full survey of 0D and 1D carbon frameworks, as well as their high-resolution Ti 2p and Fe 2p core level spectra (j).

individually explored in the following section.

To investigate the electrocatalytic activity of NO₃RR, the 3D printed carbon catalysts were tested in an H-cell under ambient conditions. As shown in the LSV curve (Fig. 2a), 0D carbon framework presents almost overlapped current density in the solution with and without KNO₃, implying its electrocatalytic inert properties towards NO₃RR. In a sharp contrast, 1D carbon framework exhibits an obvious current density enhancement from ~ -0.41 V vs. RHE compared to that in the solution without KNO₃. This suggests that 1D carbon framework possesses certain electrocatalytic activity for NO₃RR. Therefore, the NO₃RR performance is further studied at selected potentials between -0.61 and -1.61 V vs. RHE by electrolysis for 1 h (Fig. 2b). For comparison, the electrolysis was also carried out in the same manner using 0D carbon framework as working electrode. After electrolysis, the NH₃

concentration in the solution was quantified by a well-established indophenol blue colorimetric method (Fig. 2c). Although 0D carbon framework shows a moderate current density during electrolysis, the absorbances of its electrolysis solutions are significantly weak at all potentials (Fig. 2d, left panel), which is in line with its inert property towards NO₃RR reflected by LSV in Fig. 2a. Instead, a strong UV-vis absorption at 655 nm (Fig. 2d, right panel) is visualized in the electrolysis solutions from 1D carbon framework. Upon varying the potential from -0.61 and -1.61 V vs. RHE, the ammonia yield rate progressively increases from 6.8 to 364.5 $\mu\text{g h}^{-1} \text{cm}^{-2}$, and FE shows an initial upsurge from -0.61 to -0.81 V, then gradually goes beyond 50.0% at -1.21 V, and approximately stabilizes at -1.41 V (Fig. 2e). Considering both the electrolysis and energy efficiency, the durability of 1D carbon framework for NO₃RR was further explored at -1.21 V

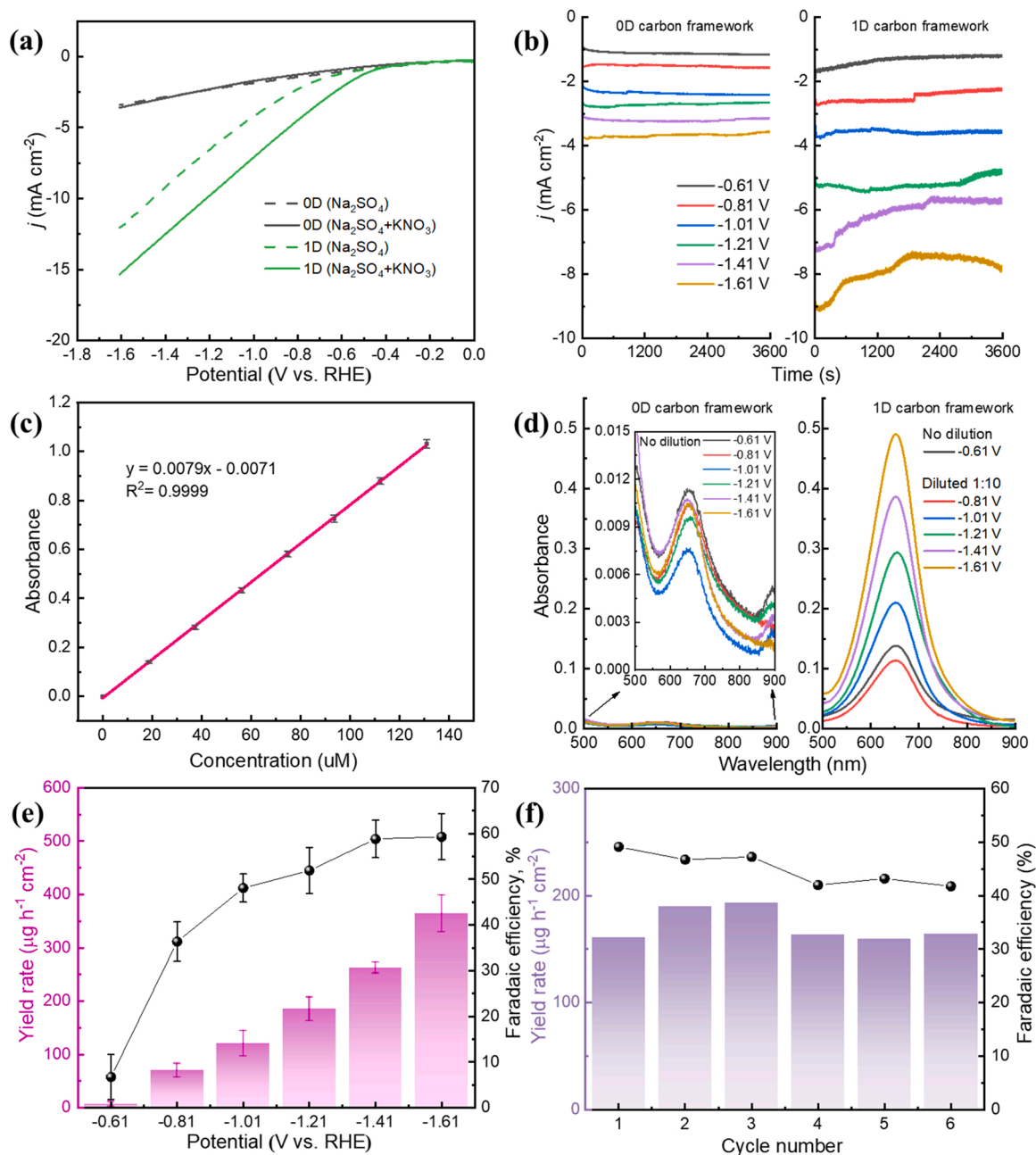


Fig. 2. (a) LSV curves of 0D and 1D carbon frameworks measured at a scan rate of 5 mV s⁻¹ in 0.5 M Na₂SO₄ electrolyte and 0.1 M KNO₃/0.5 M Na₂SO₄ mixed electrolyte. (b) Chronoamperometry curves of 0D and 1D carbon framework at different potentials. (c) Calibration curve for ammonia determination by the colorimetric indophenol blue method. (d) UV-vis absorption spectra of electrolysis solutions. (e) NH₃ yield and FE for 3D printed 1D carbon framework at different potentials. (f) The durability tests of 3D printed 1D carbon framework for NO₃RR at -1.21 V vs. RHE.

instead of more negative potentials (Fig. 2f). It shows a roughly constant electrocatalytic performance in term of both yield and FE, demonstrating the potential of 3D printed 1D carbon framework as cost-efficient electrocatalysts for electrochemical NO₃RR applications.

3.2. Electrocatalytic active sites on 1D carbon framework

To explore the possible active sites in 1D carbon framework for NO₃RR, control experiments on metal oxides impurities (TiO₂ and Fe₃O₄) and carbon defects (basal plane vs. edge plane) were considered. Specifically, the NO₃RR performance of TiO₂ and Fe₃O₄ was individually studied at selected potential of -1.21 V by dispersing TiO₂ and Fe₃O₄ on glassy carbon with a loading of ~ 0.17 mg cm⁻². As shown in Fig. S2, Fe₃O₄ shows higher current response during electrolysis with multiple sawtooth oscillations compared to approximately constant current response on TiO₂ electrode. This is due to the periodical gas bubble formation and break-up on the Fe₃O₄ electrode, which can be clearly visualized during electrolysis. Such gas bubble formation and break-up can block and recover the access of electrolyte to the surface of Fe₃O₄ electrode, leading to the continuous current fluctuations. Notably, both TiO₂ and Fe₃O₄ present a higher yield rate (1300.9 and 6078.4 $\mu\text{g h}^{-1} \text{cm}^{-2}$) and FE (60.1% and 73.0%) at -1.21 V (Fig. 3a), compared to 1D carbon framework with a yield rate of 185.3 $\mu\text{g h}^{-1} \text{cm}^{-2}$ and FE of 51.9% at the same potential. Importantly, the highly effective NO₃RR behavior of Fe₃O₄ further implies its non-negligible electrocatalytic role in 1D carbon framework in spite of its trace content as evidenced by ICP-OES (Fig. 1h).

Furthermore, defects have been demonstrated to possess a strong influence on the chemical activity of carbon materials and make defective carbon materials potential catalysts [61]. Specifically, the edge plane has been considered more electrochemically active than

basal plane due to the abrupt lattice termination, resulting in the sp³ sites, dangling bonds, and functional groups, but the basal plane also displays a non-negligible electrochemical activity [62–64]. It is therefore fundamentally important to elucidate the effect of defects on the electrochemical NO₃RR. Raman spectroscopy was invited to probe defects/disorder in 1D carbon framework. As presented in Fig. S3, a strong D band (1338 cm^{-1}) was clearly observed, demonstrating the presence of defects/disorder in 1D carbon framework [65]. To evaluate the electrocatalytic activity of carbon defects/disorder, the commercially available PGEb and PGEe were used. The LSV profile (Fig. 3b) shows that the current density of both PGEb and PGEe increases in the presence of nitrate at almost the same onset potential (~ -0.61 V vs. RHE). This implies that both PGEb and PGEe electrodes are electrocatalytically active for NO₃RR. Additionally, as the potential becomes more negative, a significantly higher current density is observed on PGEe electrode. Further electrolysis experiments performed at selected potentials of -1.21 V (Fig. S4) reveal that PGEe can produce a ~ 3.2 -fold higher NH₃ yield than PGEb with a comparable FE (42.1 vs. 36.8%), as shown in Fig. 3c. This illustrates that defects can drastically enhance the NH₃ yield rate but have limited effect on FE. Such electrocatalytic NO₃RR difference between PGEe and PGEb is related to the electrochemically active surface area (ECSA), which was further estimated based on the electrochemical double-layer capacitance. As presented in Fig. S5, The ESCA value of PGEe is 0.153 cm^2 , ~ 3.7 -fold higher than PGEb (0.041 cm^2), which is roughly proportional to the NH₃ yield increase. This verifies that PGEb and PGEe share comparable intrinsic activity towards NO₃RR. Altogether, it is deduced that pristine 1D carbon framework is intrinsically active for electrochemical NO₃RR. The defective carbon nanotubes can produce higher NH₃ yield rate due to higher ESCA, while the presence of metallic impurities can significantly enhance the electrocatalytic NO₃RR performance, rendering 1D

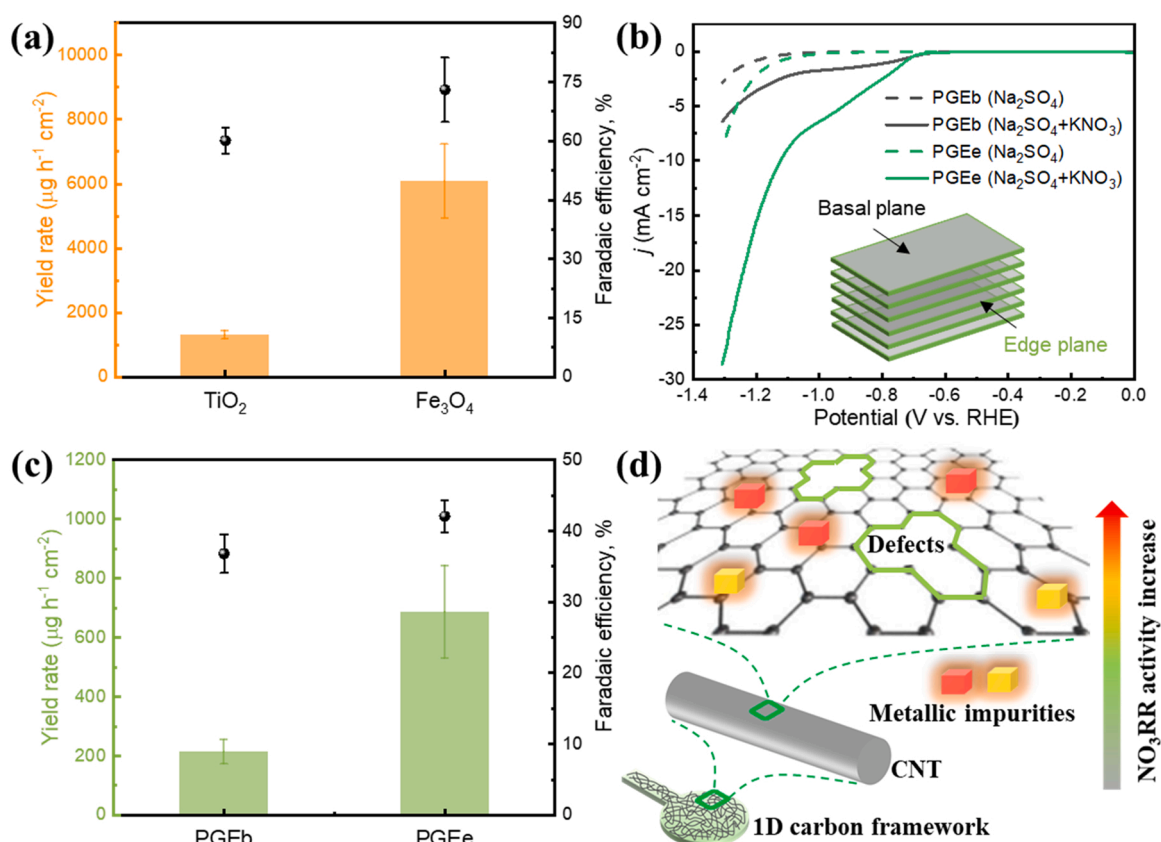


Fig. 3. (a) NH₃ yield and FE for metallic impurities in 1D carbon framework at -1.21 V. (b) LSV curves of graphite with different plane orientations measured at a scan rate of 5 mV s^{-1} in $0.5 \text{ M Na}_2\text{SO}_4$ electrolyte and $0.1 \text{ M KNO}_3/0.5 \text{ M Na}_2\text{SO}_4$ mixed electrolyte, and corresponding (c) NH₃ yield and FE at -1.21 V. (d) Schematic illustrations of NO₃RR activity for 1D carbon framework.

carbon framework analogue to metallic impurities coupled carbon substrate (Fig. 3d).

3.3. Preparation and characterization of 1D@MnO_x catalysts

However, the content and distribution of these metallic impurities in commercial carbon materials are unpredictable. To further improve the NO₃RR activity of 1D carbon framework with controllable performance, an ultrathin layer of MnO_x was coated on its surface by ALD (Fig. 4a) considering that the atomic layer coated functional materials can serve as an ultrathin active shell for electrocatalysis without sacrificing the porosity of 1D carbon framework accessible to the electrolyte. The porosity of 1D carbon framework is well remained without evident morphological changes after ALD process of MnO_x (Fig. S6). XPS wide spectrum verifies the existence of Mn on the surface of 1D@ 300-MnO_x electrode (Fig. S7a) compared to the 1D carbon framework substrate, implying the successful deposition of MnO_x. Additionally, the strong signal of Ti impurities in 1D carbon framework substrate is remarkably suppressed after MnO_x deposition. This agrees well with the formation of MnO_x shell covering the conductive carbon nanotube core. The deconvoluted high-resolution Mn-2p spectrum (Fig. S7b) reveals different oxidation states of Mn (3+ and δ+, δ ≥ 4), which are reflected by two pairs of peaks located at 642.4 and 654.3 eV, and 646.5 and 658.7 eV, respectively [66]. The presence of Mn with 3+ oxidation state is ascribed to the insufficient oxidation of Mn precursor in the O₂ plasma during ALD process.

Scanning transmission electron microscopy with a high-angle annular dark-field detector (STEM-HAADF) providing high Z-contrast imaging was performed at high acceleration voltage of 300 kV to

investigate the nanoscale structure of MnO_x coated 1D carbon framework at high resolution. After 100 ALD cycles, small MnO_x nanoclusters were observed on the surface of carbon nanotubes (Fig. S8). With increase to 300 cycles, a roughly continuous deposit of MnO_x nanoclusters is formed (Fig. S9). Further increase to 500 cycles results in a denser coating of MnO_x in the thickness of ~ 2 nm (Fig. 4b). Meanwhile, the high localized STEM electron energy loss spectroscopy (STEM-ELS) analyses (Fig. 5) performed with low acceleration voltage of 60 kV reveal clear O and Mn signals from single MnO_x nanoclusters, providing Mn/O atomic concentration ratio between 0.47 and 0.57. This signifies the formation of MnO_x with both 3+ (Mn/O = 0.67) and higher oxidation states (δ+, Mn/O ≤ 0.5). Furthermore, the Mn content from ALD-coated MnO_x was quantitatively analysed by ICP-OES measurements, increasing from ultra-low 0.0024 wt% in 1D@ 100-MnO_x to 0.0171 wt% in 1D@ 500-MnO_x (Table S1). These results, together with XPS and TEM analyses, indicate that an ultrathin MnO_x deposit could be effectively coated on the surface of 1D carbon framework by ALD, and that its thickness can be facily tuned by controlling ALD cycles. Benefiting from the sufficient electronic conductive core provided by interconnected carbon nanotubes and the electrocatalytic shell of ALD-coated MnO_x, such core-shell structures are anticipated to be effective for NO₃RR.

3.4. Electrochemical NO₃RR performance of 1D@MnO_x catalysts

The 3D@ 300-MnO_x was directly used as working electrode to investigate its electrochemical NO₃RR performance. Compared to 1D carbon framework substrate, LSV profile of 1D@ 300-MnO_x electrode

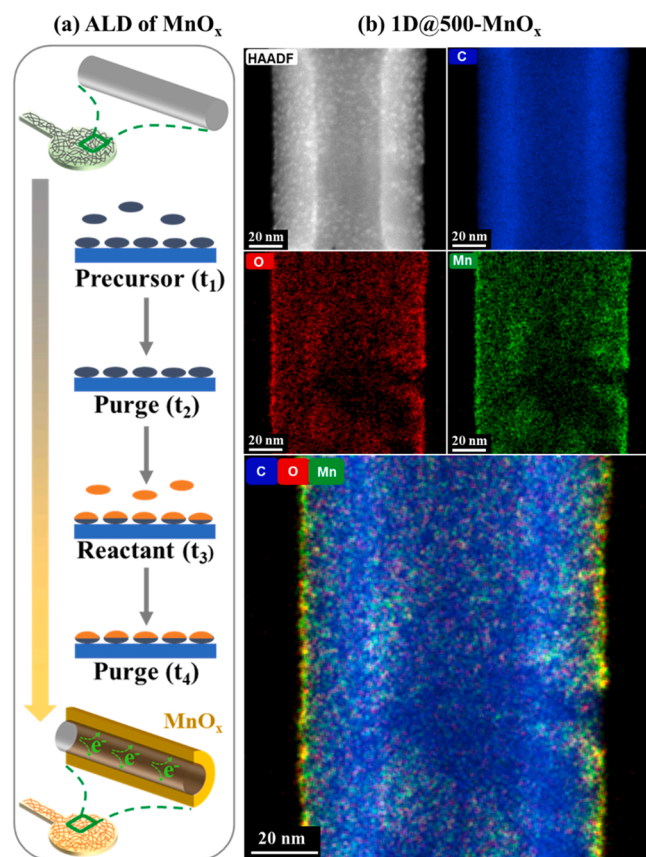


Fig. 4. (a) Schematic illustrations for fabrication of ultrathin manganese oxides coated 1D carbon framework by integration of 3D printing with ALD. (b) STEM-HAADF image of 1D@ 500-MnO_x, and corresponding STEM-EDX maps of carbon, oxygen, manganese, and an overlay of all three element maps.

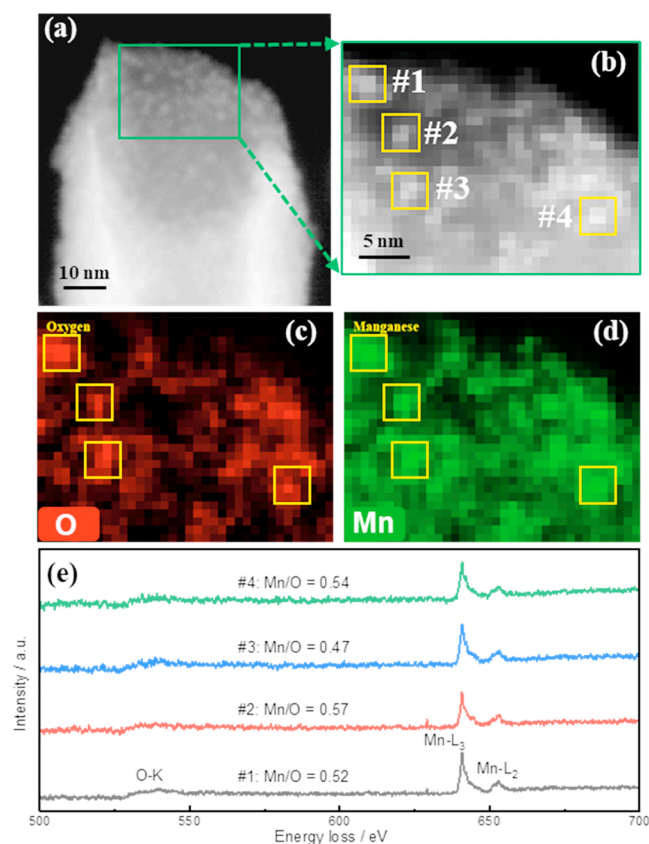


Fig. 5. STEM-ELS analyses of 1D@ 500-MnO_x electrode. (a) an overview STEM-HAADF image of one single carbon nanotube from 1D@ 500-MnO_x electrode. (b) an STEM-HAADF image and (c, d) EELS maps of O-K and Mn-L from marked zone in (a). (e) EELS spectra of four single deposited MnO_x nanoclusters with Mn/O values calculated from measured atomic concentrations of both elements.

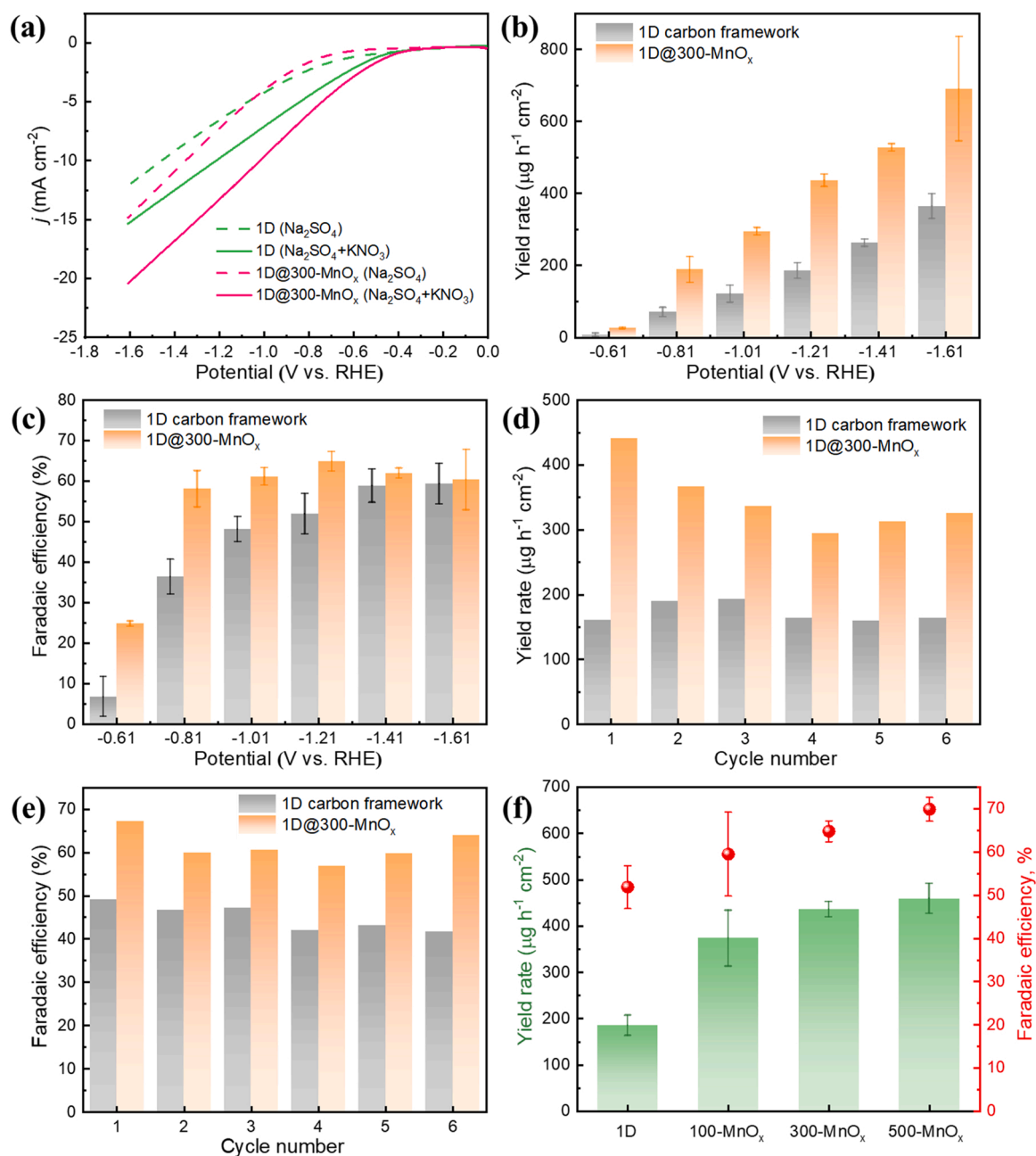


Fig. 6. (a) LSV curves of 1D@ 300-MnO_x measured at a scan rate of 5 mV s⁻¹ in 0.5 M Na₂SO₄ electrolyte and 0.1 M KNO₃/0.5 M Na₂SO₄ mixed electrolyte. (b) NH₃ yield and (c) FE of 1D@ 300-MnO_x at different potentials. (d, e) The durability tests of 1D@ 300-MnO_x for NO₃RR at -1.21 V. (f) The effect of ALD-coated MnO_x thickness on the NO₃RR performance of 1D carbon framework. For comparison, the relevant results from 1D carbon substrate are also presented in each panel.

(Fig. 6a) displays considerably enlarged current density in the electrolyte with KNO₃ than that without KNO₃, implying a more efficient NO₃RR on the surface of 1D@ 300-MnO_x electrode. Specifically, 1D@ 300-MnO_x electrode shows a current density enhancement of 6.02 mA cm⁻² in the electrolyte with KNO₃ at -1.21 V compared to that in the blank electrolyte (without KNO₃). This is approximately twice higher than that of 1D carbon framework (3.24 mA cm⁻²). Thus, Chronoamperometry measurements were further carried out to evaluate the effect of this ultrathin deposit of MnO_x on the electrochemical NO₃RR towards NH₃ synthesis (Fig. S10). Notably, 1D@ 300-MnO_x shows a significant increase in the NH₃ yields at each potential compared to 1D carbon framework (Fig. 6b). For example, a yield rate of 435.9 μg h⁻¹ cm⁻² can be obtained at -1.21 V, which is around 2.4-fold higher than 1D carbon framework at the same potential. Besides, the FE increases especially at more positive potentials such as -0.61

and -0.81 V compared to 1D carbon framework and presents a volcanic shape with a maximum value of 64.8% at -1.21 V (Fig. 6c), corresponding to the energy efficiency of 14.3% (Fig. S11). Importantly, to ensure the electrocatalytic reliability of the 1D@ 300-MnO_x, control experiments were performed by ¹⁵N-labeled NO₃ and electrolysis using blank electrolyte (Fig. S12). The typical double peaks of ¹⁵NH₄⁺ appear in ¹H NMR spectra, whereas no signal is detected if only blank solution is used during the electrolysis, which verifies that the produced NH₃ is derived from the NO₃ electroreduction. Besides, NH₃ cannot be detected under UV-vis spectroscopy when KNO₃ is absent in the electrolyte during the electrolysis. This excludes the NH₃ contamination during the experiment. Additionally, as one of the major by-products during NO₃RR process, NO₂ presents a close FE between 1D@ 300-MnO_x and 1D carbon framework (Fig. S13), indicating the NO₃ reduction to NO₂ is not significantly enhanced after coating MnO_x on 3D printed carbon

framework. Considering the ultra-low loading of ALD-coated MnO_x , which is even more than one order of magnitude lower than the trace Fe impurities in 1D@ 300- MnO_x electrode (Table S1), such electrocatalytic activity improvement in terms of both yield and FE clearly demonstrates the effectiveness of ALD-coated ultrathin MnO_x for enhancing the electrochemical NO_3RR performance of 1D carbon framework. It is believed that such electrocatalytic improvement is primarily from Mn (3+), instead of Mn with higher oxidation states (δ^+). This is because Mn (δ^+) can be readily reduced to Mn (3+) under the potential used in current study, which is exemplified by the electrolysis at -1.21 V for 5 min (Fig. S14). Besides, 1D@ 300- MnO_x electrode also presents a good durability, as reflected by the roughly stable yield rate and FE after two electrolysis cycles (Fig. 6d and e). Meanwhile, we also explored the influence of MnO_x thickness controlled by the ALD cycles on the electrochemical NO_3RR performance of 1D carbon framework (Fig. S15). Impressively, only after 100 ALD cycles (corresponding to an ultra-low Mn loading of 0.0024 wt%, Table S1), the yield rate undergoes a significant upsurge from 185.3 to 373.6 $\mu\text{g h}^{-1} \text{cm}^{-2}$, which approximately stabilizes at 435.8 $\mu\text{g h}^{-1} \text{cm}^{-2}$ after 300 cycles with a slight increase to 459.4 $\mu\text{g h}^{-1} \text{cm}^{-2}$ after 500 cycles. This indirectly verifies that a roughly continuous deposit of MnO_x nanoclusters can be formed on the surface of 1D carbon framework after 300 ALD cycles. Correspondingly, the FE also shows a considerable increase from 51.9% for 1D carbon framework to 69.9% after 500 ALD cycles of MnO_x coating (Fig. 6f). This offers a promising protocol for the functionalization of 3D-printed 1D carbon frameworks for electrocatalytic applications, favorably competing with other electrocatalysts especially in terms of large scalability (Table S2).

4. Conclusion

Inspired by the recent advances in 3D printed carbon electrocatalysts, we have explored the electrocatalytic activity of two commonly used carbon materials in 3D printing towards electrochemical NO_3RR . In contrast to the inert property of 0D counterpart, 1D carbon framework consisting of entangled carbon nanotubes shows the electrocatalytic activity of NO_3RR to NH_3 . Further studies show that the carbon nanotubes are intrinsically active for electrochemical NO_3RR . Although defects have limited effect on FE, yet defective carbon nanotubes can produce a much higher NH_3 yield due to its higher electrochemically active surface area. Besides, the inherent metallic impurities in industrially available carbon filaments represented by TiO_2 and Fe_3O_4 can exert significant influence on the electrocatalytic performance of 1D carbon framework owing to their high activity. Since the amount and distribution of these impurities are unpredictable and highly varied in different industrial fabrications, an ultrathin active deposit of MnO_x is therefore ALD-coated on the surface of 1D carbon framework, remarkably enhancing the electrochemical NO_3RR . Importantly, the thickness of this active deposit can be effectively controlled to tune the electrocatalytic properties of 3D printed carbon frameworks. This demonstrates the promising prospect of 3D printing of carbon frameworks integrated with ALD of active layers for electrocatalytic electrode fabrication.

CRedit authorship contribution statement

Wanli Gao and Martin Pumera conceived and designed the project. Wanli Gao performed the materials synthesis and characterization. Wanli Gao and Juan V. Perales-Rondon performed electrochemical measurements and data analyses. Jan Michalička performed the TEM measurements and analyses. Martin Pumera supervised the project. All authors participated in editing the final manuscript.

Declaration of Competing Interest

The authors declare that they have no known competing financial interests or personal relationships that could have appeared to influence

the work reported in this paper.

Data Availability

Data will be made available on request.

Acknowledgements

M. P. was supported by Grant Agency of the Czech Republic (GACR EXPRO: 19-26896X). W. G. was supported by the ESF under the project CZ.02.2.69/0.0/0.0/20_079/0017436. Material characterizations were carried out with the support of CzechNanoLab Research Infrastructure (ID LM2018110, MEYS CR, 2020–2022). The authors gratefully thank Dr. Stanislava Matejkova and Martin Loula for IPC-OES measurements and analyses.

Appendix A. Supporting information

Supplementary data associated with this article can be found in the online version at doi:10.1016/j.apcatb.2023.122632.

References

- [1] A. Klerke, C.H. Christensen, J.K. Nørskov, T. Vegge, Ammonia for hydrogen storage: challenges and opportunities, *J. Mater. Chem.* 18 (2008) 2304–2310, <https://doi.org/10.1039/b720020j>.
- [2] G.-F. Chen, Y. Yuan, H. Jiang, S.-Y. Ren, L.-X. Ding, L. Ma, T. Wu, J. Lu, H. Wang, Electrochemical reduction of nitrate to ammonia via direct eight-electron transfer using a copper–molecular solid catalyst, *Nat. Energy* 5 (2020) 605–613, <https://doi.org/10.1038/s41560-020-0654-1>.
- [3] H. Chen, J. Liang, K. Dong, L. Yue, T. Li, Y. Luo, Z. Feng, N. Li, M.S. Hamdy, A. A. Alshehri, Y. Wang, X. Sun, Q. Liu, Ambient electrochemical N_2 -to- NH_3 conversion catalyzed by TiO_2 decorated Juncus effusus-derived carbon microtubes, *Inorg. Chem. Front.* 9 (2022) 1514–1519, <https://doi.org/10.1039/d2qi00140c>.
- [4] G. Meng, M. Jin, T. Wei, Q. Liu, S. Zhang, X. Peng, J. Luo, X. Liu, MoC nanocrystals confined in N-doped carbon nanosheets toward highly selective electrocatalytic nitric oxide reduction to ammonia, *Nano Res.* 15 (2022) 8890–8896, <https://doi.org/10.1007/s12274-022-4747-y>.
- [5] D.R. MacFarlane, P.V. Cherepanov, J. Choi, B.H.R. Suryanto, R.Y. Hodgetts, J. M. Bakker, F.M. Ferrero Vallana, A.N. Simonov, A roadmap to the ammonia economy, *Joule* 4 (2020) 1186–1205, <https://doi.org/10.1016/j.joule.2020.04.004>.
- [6] S. Garcia-Segura, M. Lanzarini-Lopes, K. Hristovski, P. Westerhoff, Electrocatalytic reduction of nitrate: Fundamentals to full-scale water treatment applications, *Appl. Catal. B: Environ.* 236 (2018) 546–568, <https://doi.org/10.1016/j.apcatb.2018.05.041>.
- [7] P.H. van Langevelde, I. Katsounaros, M.T.M. Koper, Electrocatalytic nitrate reduction for sustainable ammonia production, *Joule* 5 (2021) 290–294, <https://doi.org/10.1016/j.joule.2020.12.025>.
- [8] S. Li, P. Ma, C. Gao, L. Liu, X. Wang, M. Shakouri, R. Chernikov, K. Wang, D. Liu, R. Ma, J. Wang, Reconstruction-induced NiCu-based catalysts towards paired electrochemical refining, *Energy Environ. Sci.* 15 (2022) 3004–3014, <https://doi.org/10.1039/d2ee00461e>.
- [9] J. Liang, Q. Liu, A.A. Alshehri, X. Sun, Recent advances in nanostructured heterogeneous catalysts for N-cycle electrocatalysis, *Nano Res. Energy* 1 (2022), e9120010, <https://doi.org/10.26599/nre.2022.9120010>.
- [10] Z. Li, Z. Deng, L. Ouyang, X. Fan, L. Zhang, S. Sun, Q. Liu, A.A. Alshehri, Y. Luo, Q. Kong, X. Sun, CeO_2 nanoparticles with oxygen vacancies decorated N-doped carbon nanorods: A highly efficient catalyst for nitrate electroreduction to ammonia, *Nano Res.* 15 (2022) 8914–8921, <https://doi.org/10.1007/s12274-022-4863-8>.
- [11] Z. Deng, C. Ma, X. Fan, Z. Li, Y. Luo, S. Sun, D. Zheng, Q. Liu, J. Du, Q. Lu, B. Zheng, X. Sun, Construction of CoP/ TiO_2 nanoarray for enhanced electrochemical nitrate reduction to ammonia, *Mater. Today Phys.* 28 (2022), 100854, <https://doi.org/10.1016/j.mtphys.2022.100854>.
- [12] Q. Chen, J. Liang, Q. Liu, K. Dong, L. Yue, P. Wei, Y. Luo, Q. Liu, N. Li, B. Tang, A. A. Alshehri, M.S. Hamdy, Z. Jiang, X. Sun, Co nanoparticle-decorated pomelo-peel-derived carbon enabled high-efficiency electrocatalytic nitrate reduction to ammonia, *Chem. Commun.* 58 (2022) 4259–4262, <https://doi.org/10.1039/d2cc00952h>.
- [13] P. Shen, G. Wang, K. Chen, J. Kang, D. Ma, K. Chu, Selenium-vacancy-rich WSe_2 for nitrate electroreduction to ammonia, *J. Colloid Interf. Sci.* 629 (2023) 563–570, <https://doi.org/10.1016/j.jcis.2022.09.012>.
- [14] Y.J. Luo, K. Chen, P. Shen, X.C. Li, X.T. Li, Y.H. Li, K. Chu, B-doped MoS_2 for nitrate electroreduction to ammonia, *J. Colloid Interf. Sci.* 629 (2023) 950–957, <https://doi.org/10.1016/j.jcis.2022.09.049>.
- [15] A.C.A. De Voors, R.A. Van Santen, J.A.R. Van Veen, Electrocatalytic reduction of NO_3 on palladium/copper electrodes, *J. Mol. Catal. A* 154 (2000) 203–215, [https://doi.org/10.1016/S1381-1169\(99\)00375-1](https://doi.org/10.1016/S1381-1169(99)00375-1).

- [16] S.E. Bae, K.L. Stewart, A.A. Gewirth, Nitrate adsorption and reduction on Cu(100) in acidic solution, *J. Am. Chem. Soc.* 129 (2007) 10171–10180, <https://doi.org/10.1021/ja071330n>.
- [17] Y. Zhao, Y. Liu, Z. Zhang, Z. Mo, C. Wang, S. Gao, Flower-like open-structured polycrystalline copper with synergistic multi-crystal plane for efficient electrocatalytic reduction of nitrate to ammonia, *Nano Energy* 97 (2022), 107124, <https://doi.org/10.1016/j.nanoen.2022.107124>.
- [18] J.-X. Liu, D. Richards, N. Singh, B.R. Goldsmith, Activity and selectivity trends in electrocatalytic nitrate reduction on transition metals, *ACS Catal.* 9 (2019) 7052–7064, <https://doi.org/10.1021/acscatal.9b02179>.
- [19] X. Fu, X. Zhao, X. Hu, K. He, Y. Yu, T. Li, Q. Tu, X. Qian, Q. Yue, M.R. Wasielewski, Y. Kang, Alternative route for electrochemical ammonia synthesis by reduction of nitrate on copper nanosheets, *Appl. Mater. Today* 19 (2020), 100620, <https://doi.org/10.1016/j.apmt.2020.100620>.
- [20] Q. Hu, Y. Qin, X. Wang, Z. Wang, X. Huang, H. Zheng, K. Gao, H. Yang, P. Zhang, M. Shao, C. He, Reaction intermediate-mediated electrocatalytic synthesis favors specified facet and defect exposure for efficient nitrate–ammonia conversion, *Energy Environ. Sci.* 14 (2021) 4989–4997, <https://doi.org/10.1039/d1ee01731d>.
- [21] J. Li, J. Gao, T. Feng, H. Zhang, D. Liu, C. Zhang, S. Huang, C. Wang, F. Du, C. Li, C. Guo, Effect of supporting matrixes on performance of copper catalysts in electrochemical nitrate reduction to ammonia, *J. Power Sources* 511 (2021), 230463, <https://doi.org/10.1016/j.jpowsour.2021.230463>.
- [22] Z.Y. Wu, M. Karamad, X. Yong, Q. Huang, D.A. Cullen, P. Zhu, C. Xia, Q. Xiao, M. Shakouri, F.Y. Chen, J.Y.T. Kim, Y. Xia, K. Heck, Y. Hu, M.S. Wong, Q. Li, I. Gates, S. Siahrostami, H. Wang, Electrochemical ammonia synthesis via nitrate reduction on Fe single atom catalyst, *Nat. Commun.* 12 (2021) 2870, <https://doi.org/10.1038/s41467-021-23115-x>.
- [23] X. Deng, Y. Yang, L. Wang, X.Z. Fu, J.L. Luo, Metallic Co nanoarray catalyzes selective NH₃ production from electrochemical nitrate reduction at current densities exceeding 2 A cm⁻², *Adv. Sci.* 8 (2021), 2004523, <https://doi.org/10.1002/adv.202004523>.
- [24] J. Lim, C.-Y. Liu, J. Park, Y.-H. Liu, T.P. Senfite, S.W. Lee, M.C. Hatzell, Structure sensitivity of Pd facets for enhanced electrochemical nitrate reduction to ammonia, *ACS Catal.* 11 (2021) 7568–7577, <https://doi.org/10.1021/acscatal.1c01413>.
- [25] R. Jia, Y. Wang, C. Wang, Y. Ling, Y. Yu, B. Zhang, Boosting selective nitrate electroreduction to ammonium by constructing oxygen vacancies in TiO₂, *ACS Catal.* 10 (2020) 3533–3540, <https://doi.org/10.1021/acscatal.9b05260>.
- [26] X. Fan, L. Xie, J. Liang, Y. Ren, L. Zhang, L. Yue, T. Li, Y. Luo, N. Li, B. Tang, Y. Liu, S. Gao, A.A. Alshehri, Q. Liu, Q. Kong, X. Sun, In situ grown Fe₃O₄ particle on stainless steel: A highly efficient electrocatalyst for nitrate reduction to ammonia, *Nano Res.* 15 (2021) 3050–3055, <https://doi.org/10.1007/s12274-021-3951-5>.
- [27] L. Hu, A. Khaniya, J. Wang, G. Chen, W.E. Kaden, X. Feng, Ambient electrochemical ammonia synthesis with high selectivity on Fe/Fe oxide catalyst, *ACS Catal.* 8 (2018) 9312–9319, <https://doi.org/10.1021/acscatal.8b02585>.
- [28] R. Wang, Z. Wang, X. Xiang, R. Zhang, X. Shi, X. Sun, MnO₂ nanoarrays: an efficient catalyst electrode for nitrite electroreduction toward sensing and NH₃ synthesis applications, *Chem. Commun.* 54 (2018) 10340–10342, <https://doi.org/10.1039/c8cc05837g>.
- [29] Y. Wang, S. Shu, M. Peng, L. Hu, X. Lv, Y. Shen, H. Gong, G. Jiang, Dual-site electrocatalytic nitrate reduction to ammonia on oxygen vacancy-enriched and Pd-decorated MnO₂ nanosheets, *Nanoscale* 13 (2021) 17504–17511, <https://doi.org/10.1039/d1nr04962c>.
- [30] L. Xie, Q. Liu, S. Sun, L. Hu, L. Zhang, D. Zhao, Q. Liu, J. Chen, J. Li, L. Ouyang, A. A. Alshehri, M.S. Hamdy, Q. Kong, X. Sun, High-efficiency electrosynthesis of ammonia with selective reduction of nitrate in neutral media enabled by self-supported Mn₂CoO₄ nanoarray, *ACS Appl. Mater. Interfaces* 14 (2022) 33242–33247, <https://doi.org/10.1021/acsaami.2c07818>.
- [31] G.A. Cerrón-Calle, A.S. Fajardo, C.M. Sánchez-Sánchez, S. García-Segura, Highly reactive Cu–Pt bimetallic 3D-electrocatalyst for selective nitrate reduction to ammonia, *Appl. Catal. B Environ.* 302 (2022), 120844, <https://doi.org/10.1016/j.apcatb.2021.120844>.
- [32] Q. Liu, L. Xie, J. Liang, Y. Ren, Y. Wang, L. Zhang, L. Yue, T. Li, Y. Luo, N. Li, B. Tang, Y. Liu, S. Gao, A.A. Alshehri, I. Shakir, P.O. Agboola, Q. Kong, Q. Wang, D. Ma, X. Sun, Ambient ammonia synthesis via electrochemical reduction of nitrate enabled by NiCo₂O₄ nanowire array, *Small* 18 (2022), 2106961, <https://doi.org/10.1002/smll.202106961>.
- [33] H. Liu, X. Lang, C. Zhu, J. Timoshenko, M. Ruscher, L. Bai, N. Guijarro, H. Yin, Y. Peng, J. Li, Z. Liu, W. Wang, B.R. Cuenya, J. Luo, Efficient electrochemical nitrate reduction to ammonia with copper-supported rhodium cluster and single-atom catalysts, *Angew. Chem.* 61 (2022), e202202556, <https://doi.org/10.1002/anie.202202556>.
- [34] W. He, J. Zhang, S. Dieckhofer, S. Varhade, A.C. Brix, A. Lielpetere, S. Seisel, J.R. C. Junqueira, W. Schuhmann, Splicing the active phases of copper/cobalt-based catalysts achieves high-rate tandem electroreduction of nitrate to ammonia, *Nat. Commun.* 13 (2022) 1129, <https://doi.org/10.1038/s41467-022-28728-4>.
- [35] Y.P. Zhu, C. Guo, Y. Zheng, S.Z. Qiao, Surface and interface engineering of noble-metal-free electrocatalysts for efficient energy conversion processes, *Acc. Chem. Res.* 50 (2017) 915–923, <https://doi.org/10.1021/acs.accounts.6b00635>.
- [36] Z. Wang, C. Sun, X. Bai, Z. Wang, X. Yu, X. Tong, Z. Wang, H. Zhang, H. Pang, L. Zhou, W. Wu, Y. Liang, A. Khosla, Z. Zhao, Facile synthesis of carbon nanobelts decorated with Cu and Pd for nitrate electroreduction to ammonia, *ACS Appl. Mater. Interfaces* 14 (2022) 30969–30978, <https://doi.org/10.1021/acsaami.2c09357>.
- [37] Y. Li, S. Xiao, X. Li, C. Chang, M. Xie, J. Xu, Z. Yang, A robust metal-free electrocatalyst for nitrate reduction reaction to synthesize ammonia, *Mater. Today Phys.* 19 (2021), 100431, <https://doi.org/10.1016/j.mtphys.2021.100431>.
- [38] N.J. Harmon, C.L. Rooney, Z. Tao, B. Shang, N. Raychaudhuri, C. Choi, H. Li, H. Wang, Intrinsic catalytic activity of carbon nanotubes for electrochemical nitrate reduction, *ACS Catal.* 12 (2022) 9135–9142, <https://doi.org/10.1021/acscatal.2c01144>.
- [39] X. Li, Y. Gu, S. Wu, S. Chen, X. Quan, H. Yu, Selective reduction of nitrate to ammonium over charcoal electrode derived from natural wood, *Chemosphere* 285 (2021), 131501, <https://doi.org/10.1016/j.chemosphere.2021.131501>.
- [40] J. Zhao, B. Shang, J. Zhai, N-doped graphene as an efficient metal-free electrocatalyst for indirect nitrate reduction reaction, *Nanomaterials* 11 (2021) 2418, <https://doi.org/10.3390/nano11092418>.
- [41] Q. Chen, J. Liang, L. Yue, Y. Luo, Q. Liu, N. Li, A.A. Alshehri, T. Li, H. Guo, X. Sun, CoO nanoparticle decorated N-doped carbon nanotubes: a high-efficiency catalyst for nitrate reduction to ammonia, *Chem. Commun.* 58 (2022) 5901–5904, <https://doi.org/10.1039/d2cc00997h>.
- [42] W. Yu, J. Yu, Y. Wang, X. Li, Y. Wang, H. Yuan, X. Zhang, H. Liu, W. Zhou, Electrocatalytic upcycling of nitrate and hydrogen sulfide via a nitrogen-doped carbon nanotubes encapsulated iron carbide electrode, *Appl. Catal. B Environ.* 310 (2022), 121291, <https://doi.org/10.1016/j.apcatb.2022.121291>.
- [43] L. Cheng, T. Ma, B. Zhang, L. Huang, W. Guo, F. Hu, H. Zhu, Z. Wang, T. Zheng, D.-T. Yang, C.-K. Siu, Q. Liu, Y. Ren, C. Xia, B.Z. Tang, R. Ye, Steering the topological defects in amorphous laser-induced graphene for direct nitrate-to-ammonia electroreduction, *ACS Catal.* 12 (2022) 11639–11650, <https://doi.org/10.1021/acscatal.2c03219>.
- [44] C. Zhu, T. Liu, F. Qian, W. Chen, S. Chandrasekaran, B. Yao, Y. Song, E.B. Duoss, J. D. Kuntz, C.M. Spadaccini, M.A. Worsley, Y. Li, 3D printed functional nanomaterials for electrochemical energy storage, *Nano Today* 15 (2017) 107–120, <https://doi.org/10.1016/j.nantod.2017.06.007>.
- [45] C.L. Manzanarez Palenzuela, F. Novotny, P. Krupicka, Z. Sofer, M. Pumera, 3D-printed graphene/poly(lactic acid) electrodes promise high sensitivity in electroanalysis, *Anal. Chem.* 90 (2018) 5753–5757, <https://doi.org/10.1021/acs.analchem.8b00083>.
- [46] J. Muñoz, E. Redondo, M. Pumera, Chiral 3D-printed bioelectrodes, *Adv. Funct. Mater.* 31 (2021), 2010608, <https://doi.org/10.1002/adfm.202010608>.
- [47] C.W. Foster, M.P. Down, Y. Zhang, X. Ji, S.J. Rowley-Neale, G.C. Smith, P.J. Kelly, C.E. Banks, 3D printed graphene based energy storage devices, *Sci. Rep.* 7 (2017) 42233, <https://doi.org/10.1038/srep42233>.
- [48] M.P. Browne, V. Urbanova, J. Plutnar, F. Novotný, M. Pumera, Inherent impurities in 3D-printed electrodes are responsible for catalysis towards water splitting, *J. Mater. Chem. A* 8 (2020) 1120–1126, <https://doi.org/10.1039/c9ta11949c>.
- [49] C.H. Wong, Z. Sofer, M. Kubesova, J. Kucera, S. Matejkova, M. Pumera, Synthetic routes contaminate graphene materials with a whole spectrum of unanticipated metallic elements, *Proc. Natl. Acad. Sci. USA* 111 (2014) 13774–13779, <https://doi.org/10.1073/pnas.1413390111>.
- [50] M. Pumera, A. Ambrosi, E.L.K. Chng, Impurities in graphenes and carbon nanotubes and their influence on the redox properties, *Chem. Sci.* 3 (2012) 3347, <https://doi.org/10.1039/c2sc21374e>.
- [51] J. Masa, W. Xia, M. Muhler, W. Schuhmann, On the role of metals in nitrogen-doped carbon electrocatalysts for oxygen reduction, *Angew. Chem. Int. Ed.* 54 (2015) 10102–10120, <https://doi.org/10.1002/anie.201500569>.
- [52] J. Lee, G.N. Tomaraei, M. Abdulhazef, M. Bedewy, Boosting catalytic lifetime in chemical vapor deposition of carbon nanotubes by rapid thermal pretreatment of alumina-supported metal nanocatalysts, *Chem. Mater.* 33 (2021) 6277–6289, <https://doi.org/10.1021/acs.chemmater.0c04692>.
- [53] F. Mattelaer, P.M. Vereecken, J. Dendooven, C. Detavernier, Deposition of MnO anode and MnO₂ cathode thin films by plasma enhanced atomic layer deposition using the Mn(thd)₃ precursor, *Chem. Mater.* 27 (2015) 3628–3635, <https://doi.org/10.1021/acs.chemmater.5b00255>.
- [54] J. Han, Y. Kim, D.H.K. Jackson, H. Chang, H.W. Kim, J. Lee, J.-R. Kim, Y. Noh, W. B. Kim, K.-Y. Lee, H.J. Kim, Enhanced catalytic performance and changed reaction chemistry for electrochemical glycerol oxidation by atomic-layer-deposited Pt-nanoparticle catalysts, *Appl. Catal. B Environ.* 273 (2020), 119037, <https://doi.org/10.1016/j.apcatb.2020.119037>.
- [55] D. Lee, Y. Kim, H. Han, W.B. Kim, H. Chang, T.-M. Chung, J.H. Han, H.W. Kim, H. J. Kim, Atomic-layer-deposited SnO₂ on Pt/C prevents sintering of Pt nanoparticles and affects the reaction chemistry for the electrocatalytic glycerol oxidation reaction, *J. Mater. Chem. A* 8 (2020) 15992–16005, <https://doi.org/10.1039/d0ta02509g>.
- [56] D. Liu, L. Qiao, Y. Chen, P. Zhou, J. Feng, C.C. Leong, K.W. Ng, S. Peng, S. Wang, W.F. Ip, H. Pan, Electrocatalytic reduction of nitrate to ammonia on low-cost manganese-incorporated Co₃O₄ nanotubes, *Appl. Catal. B Environ.* 324 (2023), 122293, <https://doi.org/10.1016/j.apcatb.2022.122293>.
- [57] W. Gao, M. Pumera, 3D Printed nanocarbon frameworks for Li-ion battery cathodes, *Adv. Funct. Mater.* 31 (2021), 2007285, <https://doi.org/10.1002/adfm.202007285>.
- [58] W. Gao, J. Michalick, M. Pumera, Hierarchical atomic layer deposited V₂O₅ on 3D printed nanocarbon electrodes for high-performance aqueous zinc-ion batteries, *Small* 18 (2022), 2105572, <https://doi.org/10.1002/smll.202105572>.
- [59] T. Kolodiazny, M. Pumera, Towards an ultrasensitive method for the determination of metal impurities in carbon nanotubes, *Small* 4 (2008) 1476–1484, <https://doi.org/10.1002/smll.200800125>.
- [60] P. Li, Z. Jin, Z. Fang, G. Yu, A single-site iron catalyst with preoccupied active centers that achieves selective ammonia electrosynthesis from nitrate, *Energy Environ. Sci.* 14 (2021) 3522–3531, <https://doi.org/10.1039/d1ee00545f>.
- [61] D.W. Boukhvalov, M.I. Katsnelson, Chemical functionalization of graphene with defects, *Nano Lett.* 8 (2008) 4373, <https://doi.org/10.1021/nl802234n>.

- [62] C.E. Banks, T.J. Davies, G.G. Wildgoose, R.G. Compton, Electrocatalysis at graphite and carbon nanotube modified electrodes: edge-plane sites and tube ends are the reactive sites, *Chem. Commun.* (2005) 829–841, <https://doi.org/10.1039/b413177k>.
- [63] C.H.A. Wong, M. Pumera, On reproducibility of preparation of basal plane pyrolytic graphite electrode surface, *Electrochem. Commun.* 13 (2011) 1054–1059, <https://doi.org/10.1016/j.elecom.2011.06.033>.
- [64] M. Velický, P.S. Toth, C.R. Woods, K.S. Novoselov, R.A.W. Dryfe, Electrochemistry of the basal plane versus edge plane of graphite revisited, *J. Phys. Chem. C* 123 (2019) 11677–11685, <https://doi.org/10.1021/acs.jpcc.9b01010>.
- [65] M.S. Dresselhaus, G. Dresselhaus, R. Saito, A. Jorio, Raman spectroscopy of carbon nanotubes, *Phys. Rep.* 409 (2005) 47–99, <https://doi.org/10.1016/j.physrep.2004.10.006>.
- [66] Y. Xu, Y. Sheng, M. Wang, T. Ren, K. Shi, Z. Wang, X. Li, L. Wang, H. Wang, Interface coupling induced built-in electric fields boost electrochemical nitrate reduction to ammonia over CuO@MnO₂ core-shell hierarchical nanoarrays, *J. Mater. Chem. A* 10 (2022) 16883–16890, <https://doi.org/10.1039/d2ta02006h>.